

3D helical CT Reconstruction with a Memory Efficient Learned Primal-Dual Architecture

Jevgenija Rudzusika*

Department of Mathematics
KTH Royal Institute of Technology
Sweden
jevaks@kth.se

Buda Bajić †

Faculty of Technical Sciences
University of Novi Sad
Serbia
buda.bajic@uns.ac.rs

Thomas Koehler

Philips Research
Germany
thomas.koehler@philips.com

Ozan Öktem

Department of Mathematics
KTH Royal Institute of Technology
Sweden
ozan@kth.se

Abstract

Deep learning based computed tomography (CT) reconstruction has demonstrated outstanding performance on simulated 2D low-dose CT data. This applies in particular to domain adapted neural networks, which incorporate a handcrafted physics model for CT imaging. Empirical evidence shows that employing such architectures reduces the demand for training data and improves upon generalisation. However, their training requires large computational resources that quickly become prohibitive in 3D helical CT, which is the most common acquisition geometry used for medical imaging. Furthermore, clinical data also comes with other challenges not accounted for in simulations, like errors in flux measurement, resolution mismatch and, most importantly, the absence of the real ground truth. The necessity to have a computationally feasible training combined with the need to address these issues has made it difficult to evaluate deep learning based reconstruction on clinical 3D helical CT. This paper modifies a domain adapted neural network architecture, the Learned Primal-Dual (LPD), so that it can be trained and applied to reconstruction in this setting. We achieve this by splitting the helical trajectory into sections and applying the unrolled LPD iterations to those sections sequentially. To the best of our knowledge, this work is the first to apply an unrolled deep learning architecture for reconstruction on full-sized clinical data, like those in the Low dose CT image and projection data set (LDCT). Moreover, training and testing is done on a single GPU card with 24GB of memory.

*Supported by Swedish Foundation of Strategic Research grant AM13-0049, grant from the VINNOVA Open Innovation Hub project 2015-06759 and by Philips Healthcare.

†Supported by Ministry of Education, Science and Technological Development of the Republic of Serbia, project ON174008.

This work has been submitted to the IEEE for possible publication. Copyright may be transferred without notice, after which this version may no longer be accessible.

1 Introduction

Clinical computed tomography (CT) aims to computationally recover an image representing the interior anatomy of a subject by taking X-ray projections from different directions.

Early approaches were inherently 2D in the sense that they aimed to recover a specific 2D cross section of the subject. To get a 3D image required one to repeat this for multiple adjacent 2D cross sections (step and shoot method). A major advance for 3D imaging came in the late 1980s with the introduction of helical scanning [33]. Here, the subject moves continually through the gantry while the x-ray source and corresponding detector is rotating. This corresponds to having an x-ray source on a helical path around the subject. Compared to step and shoot acquisition, helical CT scanning is much faster, e.g. one can scan many organs in a single breath-hold, thus reducing pulmonary motion artefacts. Helical scanning is therefore the de facto standard acquisition method for clinical CT.

It is challenging to design reconstruction methods that are capable of taking full advantage of the data acquired in 3D helical CT *without* compromising on computational feasibility. This is mostly due to the combination of having a complicated acquisition geometry and the large scale nature of the problem, the arrays for storing data and 3D image can in clinical 3D helical CT easily reach 10^8 – 10^9 elements.

Theoretically exact analytic reconstruction methods have fast reconstruction run-time, but they fail to make use of *all* the measured data without resorting to approximations. In contrast, model based iterative or variational approaches can use all of the data, but they have too long reconstruction run-time. Deep learning based methods form a third paradigm for reconstruction that outperform model based approaches regarding the image quality while having a reconstruction run-time that is closer to the analytic methods [4, 43, 33]. Nevertheless, the substantial demand for computational resources during training constrains the size of problems one can address without using graphics processing unit (GPU) super-computing resources and extensive software engineering.

The overall aim of this paper is to develop a deep learning based reconstruction method that (a) delivers high image quality, (b) can be trained on *high-end consumer GPU hardware*, (c) and can be applied to the clinical 3D helical CT data. We start out from the Learned Primal-Dual (LPD) architecture [1] that has shown state-of-the-art performance in 2D CT reconstruction. Our *main contributions* are the following:

- We show how to overcome technical challenges and scale up the method to be applicable to 3D helical CT. This includes finding the right balance between GPU memory and computational time required for training;
- We propose changes in the neural network architecture that are specifically suited for helical geometry and lead to additional performance gains;
- We apply the method to clinical data from the Low dose CT image and

projection (LDCT) data set. This includes bridging the gap between the real data and simulations, while dealing with the absence of the actual ground truth.

1.1 Computational feasibility

The LPD architecture is formed by truncating the iterative scheme given by the primal dual hybrid gradient (PDHG) optimization method, then replacing proximal operators with neural networks. The resulting deep neural network consists of blocks representing unrolled iterations. As with all deep neural networks, the drawback of LPD is its large GPU memory footprint during back-propagation, which is too large for end-to-end training on high-dimensional input data. It is possible to reduce the GPU memory footprint of a neural network in training at the cost of increased computational training time. The challenge is to keep the computational time within the practical limits. To exemplify, the training of our final method on a single GeForce RTX 3090 GPU with 24GB of memory required 6 weeks! Omitting any of the steps outlined below renders unfeasible training time.

Check-pointing We start with gradient check-pointing [8], i.e. saving activation values of some hidden layers during the forward pass of the network and recomputing the others during the back-propagation. However, moving the checkpoints to the central processing unit (CPU) memory leads to communication overhead, so saving layers that have many channels is inefficient, not to mention that the CPU memory also has limits. Therefore, we only save inputs and outputs of each unrolled iteration as checkpoints.

Partitioning the data The dimension of clinical tomographic data is so large that even a single unrolled LPD iteration does not fit into the memory of a high-end consumer GPU. Therefore, we partition the projection data into sections and identify the sub-volumes in the image domain that correspond to those sections. Next, we apply unrolled LPD iterations to these sub-volumes using only one data section at a time. As shown in section 4.3, this modification of the original LPD architecture is beneficial in the context of helical CT.

Training on smaller samples Even though the above steps are sufficient to process clinical projection data of any size, the training on full-sized data would take months, if not years. In order to facilitate faster training, we train against smaller samples of the projection data and corresponding 3D reconstructions. We investigate how the size of the training samples influence the performance and find that the optimal size of the projection data corresponds to two helical turns. The trained network generalizes well to much longer helical trajectories (12.5 - 36 turns in our test cases). Furthermore, we explore an alternative strategy, which leads to significant improvements: We apply the network using the same input size as it was trained for in a “sliding window” manner. The

obtained partial reconstructions are then combined using weighted averaging as described in section 3.3.

1.2 Clinical data

The main challenge in supervised training of deep learning-based reconstruction methods against real clinical CT data is the absence of the ground truth. We address this problem by training the method on simulated data and then evaluating it on the real data. We make the simulations more accurate than it is typically done by using the real acquisition geometries and noise statistics as in the LDCT data set. In particular, this means that the method is trained to implicitly handle varying pitch and data signal-to-noise ratio that occur in the clinical setting. Secondly, we apply corrections to the real data to address the remaining issues, such as, errors in flux measurement, objects outside the scans field of view and resolution mismatch. Finally, we discuss an alternative approach, i.e. using a full dose reference reconstruction as a proxy for the ground truth, in section section 5.

2 Related work

First reconstruction methods for helical 3D CT were *analytic methods* that combine back-projection with a convolution using a suitable (reconstruction) filter. Since the filter in such a method depends on the acquisition geometry, early approaches relied on approximate recovery that combines re-binning to a simplified geometry, e.g., slice-wise 2D [31] with 2D-filtered back-projection (FBP) or 3D-Feldkamp-Davis-Kress (FDK) type of analytic reconstruction (see surveys [5, 15] and [40, Table 1.2]). Novel reconstruction filters for FBP that provide theoretically exact recovery from helical CT data were introduced in 2003 [19, 20].

A fundamentally different approach is to define reconstruction as a solution to an optimization problem that involves minimizing data discrepancy and accounts for prior assumptions through additional regularizing components. These *iterative model based methods* have become increasingly popular since 2015 and are nowadays preferred over analytic reconstruction methods in clinical CT [26]. Here the acquisition geometry is explicitly encoded in the forward/back-projection model. However, arrays needed to store projection and image data in helical CT are very large, so the key challenge is to handle the computational burden. Currently, most iterative model based methods are stopped long before iterates have converged. The extensive mathematical theory that offers convergence guarantees and error estimates for many of these model based methods [35] is therefore not applicable in this setting.

Recently there is an increasing interest in data driven deep learning based approaches for CT reconstruction. Much of the development is catalysed by the possibility to significantly improve image quality in low-dose setting *without* compromising on computational feasibility. However, these methods require

extensive computational resources for adjusting free parameters during training. Given the size of the input data in helical CT, limited GPU memory is a major problem.

Certain features in an architecture of a neural network allow to reduce its memory footprint at the cost of additional computations. As an example, invertibility is a property that allows to recompute activations of intermediate layers, while performing back-propagation [12]. Inspired by this idea, [34] modified the architecture of state-of-the-art LPD method [1], so that its unrolled iterations become invertible. As a result, the memory footprint of the method was reduced to the footprint of one invertible block. [28] used invertibility combined with patch-wise evaluation of convolutional operations within the invertible blocks, which allowed to shift the balance between memory and computational time even further. The advantage of using invertible networks over gradient checkpointing is that there is no need for additional CPU-GPU communication. The drawback is that the modification likely results in reduced model capacity so its performance is expected to decrease when compared to the original LPD architecture [34]. In addition, each invertible block has to be executed three times, while each network block between the checkpoints has to be recomputed only twice. Another approach proposed in [39] was inspired by neural ordinary differential equations (ODEs) [7]. Here, a solution to a reconstruction problem is represented by a function that evolves over time and the derivative of this function is represented by a neural network. The final solution can be obtained through numerical integration, which results in repeated applications of the network with additive skip-connections. This architecture does not require storing activations of intermediate layers as the gradients can be computed by an ODE solver instead of traditional back-propagation. In this case, the memory footprint of the method is approximately equal to the footprint of the network representing the derivative. So far, all the methods described above have been applied in 3D CT reconstruction with a circular acquisition geometry. However, their application to helical geometry requires additional improvements.

Another approach to reduce the memory footprint is to reduce the amount of input data that is processed by the neural network at the same time. A natural approach for achieving this is splitting the input data into parts and down-sampling. The down-sampling strategy has been explored in [13], where learned gradient-descent is applied in different scales, starting from a coarse reconstruction and then gradually increasing resolution to reconstruct small details. However, since the proposed architecture involves a block that acts on the full resolution, the memory footprint of this method is still large.

Splitting the tomographic data is not a new concept in tomography. In ordered subsets methods [17, 11, 21, 3] only a section of the data is used to update an image volume during one iteration of iterative reconstruction. This leads to initial acceleration of various optimization methods. Recently, this idea has been used to modify the LPD architecture [37] with the goal of improving computational efficiency of the method. However, Learned Stochastic Primal-Dual (LSPD) method presented in [37], relies on a stochastic choice of the section of the data, while in this work we select the sections subsequently in

order to ensure that all the data has been used (which might not be the case in a stochastic setting, given relatively few unrolled iterations).

The idea of splitting image volumes is partially explored in [44], where images are split into parts (patches) and those are used within greedy training of learned gradient-descent. However, the greedy training often leads to sub-optimal performance compared to an end-to-end approach, as it was also observed [34]. Furthermore, an approach of splitting image volumes for parallelization purposes is presented in [29]. Here, an image volume is split into non-overlapping blocks, so that only neighboring blocks share some tomographic data. This is used to split computations across multiple GPUs with reduced communication overhead. In contrast, our work in this paper focuses on performing computations on one GPU.

A computationally efficient way to use deep learning for image reconstruction in 3D is to augment an analytical reconstruction method, such as FBP, [24, 42, 23]. This can be done by learning the convolutional kernel for filtering the data and/or by applying the neural networks for pre-processing the data and post-processing the reconstruction. A lot of deep learning methods address only the post-processing step by learning the mapping between low-dose and normal-dose reconstructions obtained with analytical methods. In particular, very few works have utilized the clinical projection data in the LDCT data set [25], even fewer without re-binning to a parallel 2D geometry. One exception is [23], they trained an FBP-based architecture using an unsupervised loss in the data domain. As a result the training required neither ground truth reconstructions, nor a reference reconstruction method. As we discuss in section 5, the absence of the ground truth reconstructions is indeed an important issue to address. We find the unsupervised training strategies as in [23] to be very promising and note that it can be applied to the LPD as well. However, we leave it out of the scope of this paper.

3 Method

First, we provide the theoretical foundations for deep learning based reconstruction methods. Then we outline the original LPD architecture and describe the proposed modifications. Lastly, we propose different strategies for training and inference using helical CT data.

3.1 Theoretical foundations

Learned iterative reconstruction uses principles from statistical decision theory to learn an ‘optimal’ reconstruction method from training data [4, Section 5]. Consider a setting where one has access to supervised training data in the form of i.i.d. samples $(f_1, g_1), \dots, (f_n, g_n) \in X \times Y$ of (\mathbb{f}, \mathbb{g}) where \mathbb{f} and \mathbb{g} are X - and Y -valued random variable generating 3D images and helical CT data, respectively, and

$$\mathbb{g} = \mathcal{A}(\mathbb{f}) + \mathbb{e}. \quad (1)$$

The mapping $\mathcal{A}: X \rightarrow Y$ (ray transform) models how a 3D image gives rise to helical CT data in absence of observation errors, and the random variable e represents observation error.

Our aim is now to learn the ‘best’ reconstruction method from the above supervised training data. To proceed, one has a pre-defined parametrised family $\{\mathcal{R}_\theta\}_\theta$ of possible reconstruction methods $\mathcal{R}_\theta: Y \rightarrow X$. The ‘best’ one can be taken as a Bayes’ estimator, which for image-loss $\mathcal{L}_X: X \times X \rightarrow \mathbb{R}$ is defined as

$$\mathcal{R}_{\hat{\theta}}: Y \rightarrow X \quad \text{where} \quad \hat{\theta} \in \arg \min_{\theta} \sum_{i=1}^n \mathcal{L}_X(\mathcal{R}_\theta(g_i), f_i). \quad (2)$$

The choice of the image-loss $\mathcal{L}_X: X \times X \rightarrow \mathbb{R}$ governs the type of estimator one seeks to approximate. Choosing squared ℓ_2 -loss $\mathcal{L}_X(f, f') := \|f - f'\|_2^2$ means that the learned reconstruction method approximates the posterior mean, i.e.,

$$\mathcal{R}_{\hat{\theta}}(g) \approx \mathbb{E}[f \mid g = g] \quad \text{where} \quad \hat{\theta} \text{ is given by eq. (2).}$$

A key component is the choice of parametrisation for the family of reconstruction methods $\mathcal{R}_\theta: Y \rightarrow X$. One could select a generic deep neural network (DNN) architecture, consisting of fully connected layers, but if applied to helical CT, such architectures easily become very large due to the size of the input and output data. Training such DNNs would require vast amounts of data and the resulting learned reconstruction method, would most likely generalise poorly. An alternative approach is to adapt the DNN architecture for \mathcal{R}_θ . A basic way to do this is to consider $\mathcal{R}_\theta := \mathcal{C}_\theta \circ \mathcal{A}^\dagger$ where $\mathcal{A}^\dagger: Y \rightarrow X$ is a hand-crafted approximate inverse of \mathcal{A} and $\mathcal{C}_\theta: X \rightarrow X$ is some 3D image-to-image post-processing operator that is learned from training data. Popular architectures in imaging for the latter are based on convolutional neural networks (CNNs), like U-Net [18].

A different path to domain adaptation is through *unrolling*. The idea is to start with some iterative scheme, like one designed to minimize $f \mapsto \|\mathcal{A}(f) - g\|_2^2$. The next step is to truncate this scheme and replace the handcrafted updates with possibly shallow CNNs (unrolling). \mathcal{R}_θ is then a DNN that is formed by stacking these shallow CNNs and coupling them with \mathcal{A} and its adjoint \mathcal{A}^* , which are explicitly given [4, Sec. 4.9.1]. An example of this is the LPD method [1] and variants thereof that are described in section 3.2. Finally, note that *unrolling is merely a way to select a DNN architecture for \mathcal{R}_θ* . In particular, training as in eq. (2) will *not* yield a solution operator for an optimization problem.

3.2 Architectures

The state-of-the-art unrolling scheme for CT reconstruction is the LPD network introduced in [1]. In the following subsections, we briefly describe the original method, LPD, and technical steps that are sufficient to use this method in a 3D setting essentially without changing the architecture. Further we propose

Algorithm 1: LPD [1]³

-
- 1: Choose initial primal and dual variables
 $(f_0, u_0) = \mathbf{init}(g)$, where $(f_0, u_0) \in (X^{N_p}, Y^{N_d})$
 - 2: **For** $i = 1, 2, \dots, M$ **do**:
 - 3: Dual update: $u_i = u_{i-1} + \Gamma^i(u_{i-1}, \mathcal{A} f_{i-1}^{(2)}, y)$
 - 4: Primal update: $f_i = f_{i-1} + \Lambda^i(f_{i-1}, \mathcal{A}^* u_i^{(1)})$
 - 5: **return** $f_M^{(1)}$
-

an improvement of the method specifically suited for helical geometry, Learned Primal-Dual for helical CT (LPDh).

3.2.1 The original Learned Primal-Dual architecture

The LPD architecture is inspired by the iterative scheme in the PDHG algorithm [6]. This architecture incorporates a forward operator and its adjoint into a DNN by unrolling [27] a proximal primal-dual optimization scheme and replacing the proximal operators with CNNs. Hence, the LPD architecture is domain adapted in the sense that the forward/back-projection operators encode an explicit physics based model for CT data acquisition. More precisely, the LPD architecture is given in Algorithm 1, where M is the number of unrolling iterates, N is the total number of memory channels and superscripts (1) and (2) denote the 1st and the 2nd channel of the assigned variables. The functions Γ^i and Λ^i are CNNs that operate on the dual and the primal space, respectively. For each unrolled iteration i these networks have the same architecture but different learned parameters. To simplify notation, we suppress the explicit dependence of Γ^i and Λ^i on the learned parameters $\theta \in \Theta$.

In the original LPD paper [1], Γ^i and Λ^i are convolutional neural networks with two hidden layers and parametric Rectified Linear Unit (ReLU) activation functions. Here, we substitute the 2D convolutional layers by 3D convolutional layers and use simple ReLU activation functions, because of the possibility to evaluate the function in-place without using additional memory.

Primal and dual variables (f_0, u_0) are initialized with zeros.

Check-pointing Gradient check-pointing is an “off-the-shelf” technique to reduce the memory footprint of a neural network during the back-propagation at the cost of computational time [8]. Instead of storing activation values of the whole computational graph in memory, it is possible to save values of selected layers (checkpoints) and recompute the graph part by part from these layers. In a typical scenario, a part of the graph that has to be recomputed should fit into the GPU memory. Therefore, when the memory is limited there is an incentive to split the graph into smaller parts. Furthermore, the checkpoints

³ Note that this LPD formulation slightly differs from the one given in Alg. 3 in [1], but it still reflects the actual implementation used in experiments in [1].

can be stored in CPU memory. Unfortunately, copying the data between devices also takes time. Therefore, it is not beneficial to copy very large arrays. In the case of LPD, certain balance is achieved when the checkpoints are done between the unrolled iterations, meaning that only inputs and outputs of the neural networks Γ^i and Λ^i are saved, while all intermediate computations are recomputed. The reason is that hidden layers inside the networks have much more channels than primal and dual variables $(f_i, u_i), i = 1, \dots, M$ (typically 32 channels in the hidden layers and 5 channels for the primal and dual variables).

Splitting the layers Despite a very large reduction in memory requirements achieved with check-pointing, it is still not sufficient for training LPD on helical CT data on single GPU of standard capacity of 24 GB. The reason is that the size of a typical helical scan of an abdomen is about 7 GB, while the size of a typical reconstruction is about 200 MB. In LPD one check-pointed block (Γ^i or Λ^i) is a shallow neural network applied either in data domain or in image domain. If this network has 2 hidden layers with n channels, then the memory footprint will be at least $2n + 1$ multiplied by the size of an input (7 GB). Evidently, with such a large amount of input data, even a very shallow network does not fit into the memory. One solution is to de-parallelize a CNN by splitting the input arrays into spatial blocks and applying the network to these blocks sequentially [28]. To ensure that the output values are not affected by the splitting, it is necessary to use a small overlap between blocks. The size of this overlap depends on the field of view of the output neurons and, in case of a 3 layer CNN without strides, it is necessary to add 3 cells to each block from each side.

3.2.2 Learned Primal-Dual architecture for helical CT

Here, we propose a different approach for “de-parallelization” of a single unrolled LPD iteration. We partition the projection data into non-overlapping sections and identify the sub-volumes in the image domain that correspond to those sections. Inspired from the OS optimization methods [17], we subsequently apply unrolled LPD iterations to these sub-volumes using only one data section at a time. An advantage of this approach from the optimization perspective is that the updated part of the image serves as input to the next sub-iteration. In contrast, the original LPD uses all the projection data and then simultaneously updates all voxels in the image domain. Looking from the deep learning perspective at this approach, we can say that the connectivity between spatially distant neurons within the neural network is increased without increasing the number of network parameters. Further follows a detailed description of the method.

Each element in the tomographic data corresponds to the attenuation of a ray propagating through an object. Mathematically (before discretization and without noise) this can be seen as an integral over a line l defined in the image

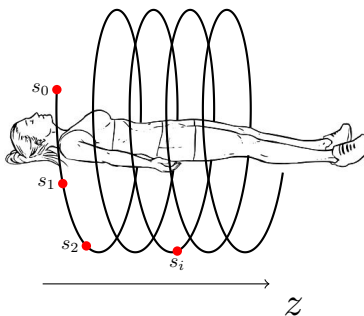


Fig. 1: Source positions $s_i \in [0, 2\pi) \times \mathbb{R}$ are described by an angle $\varphi_i \in [0, 2\pi)$ (very close to being uniform) and $z_i \in \mathbb{R}$ offset along the rotation axis (not so uniform in practice).

domain:

$$g(l) = \mathcal{A}(f)(l) = \int_l f ds. \quad (3)$$

We process only a subset of these line integrals at a time that correspond to a contiguous section of data. These lines pass through the object of interest in a limited region in the image domain. Thus, instead of applying a neural network Λ^i to the whole image volume, we apply it only to a sub-volume, which is crossed by the aforementioned lines. Further follows a formal description of our approach.

In practice, signals (images) and data measured with 3D helical CT are digitized and represented by arrays. The image space is $X = \mathbb{R}^{I_w \times I_h \times N_z}$, where I_w and I_h are image width and height, respectively, and N_z is the number of slices along the rotation axis (z -axis). Note that N_z can be different for different scans, while the other two dimensions are fixed. The data space is $Y = \mathbb{R}^{N_\varphi \times D_w \times D_h}$ where N_φ is the total number of angles/source positions and D_w and D_h correspond to the number of detector columns and detector rows, respectively. As in the image space, the number of source positions along the trajectory (N_φ) can be different, while the dimensions of the detector are fixed. Figure 1 provides a visualization of a helical trajectory of the radiation source around the patient.

We split the data space Y into sub-spaces that correspond to the data acquired from the parts of a helical trajectory:

$$Y = Y^1 \times \dots \times Y^j \times \dots \times Y^{N_s} \times Y^{N_s+1}.$$

Here, the j th data subspace is $Y^j := \mathbb{R}^{N_a \times D_w \times D_h}$, where number of angles in one part equals to N_a for $j = 1, 2, \dots, N_s$. For simplicity fix N_a and discard the data corresponding to Y^{N_s+1} , i.e. the data observed from the source at the end of the trajectory. Thus, N_s is the number of complete subspaces of the same dimension. We split the (truncated) data accordingly:

$$g = (g^1, g^2, \dots, g^{N_s}).$$

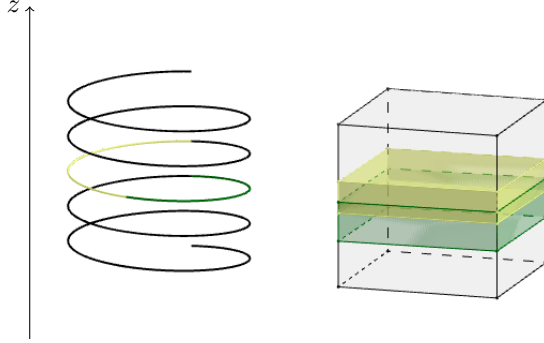


Fig. 2: An illustration of splitting helical data (left) and image volume (right). One image sub-volume (a cube on the right) corresponds to the data obtained from the source positions on the helix marked with the same color (on the left). Note that image sub-volumes overlap, while data is partitioned without overlaps.

Next, for each section of data, we consider a corresponding region in the image domain, from which this data has been obtained. Thus, from one image volume f we extract N_s overlapping sub-volumes

$$(f^1, f^2, \dots, f^{N_s}) \quad \text{where } f^j \in X^j \text{ for } j = 1, \dots, N_s.$$

Each image subspace is $X^j = \mathbb{R}^{I_w \times I_h \times N_t}$, where N_t is the minimal thickness of image sub-volume obtained by adding the physical detector height and the largest pitch. In this case, image subspace X^j contains all the line segments necessary to compute the data in subspace Y^j . Note that the image sub-volumes f^j overlap, but the data sections g^j do not (see visualization in fig. 2).

We now define the restriction of the forward operator $\mathcal{A}: X \rightarrow Y$ to X^j as

$$\mathcal{A}^j: X^j \mapsto Y^j,$$

i.e., it is an intersection of rows and columns from \mathcal{A} corresponding to the j th data section and the j th sub-volume, respectively. Next, we define projection operators

$$\mathcal{P}_{X^j}: X \mapsto X^j, \quad \text{s.t.} \quad \mathcal{P}_{X^j}(f) = f^j$$

and

$$\mathcal{P}_{Y^j}: Y \mapsto Y^j, \quad \text{s.t.} \quad \mathcal{P}_{Y^j}(g) = g^j.$$

Lastly, we define zero padding operators

$$\tilde{\mathcal{P}}_{X^j}: X^j \mapsto X, \quad \text{and} \quad \tilde{\mathcal{P}}_{Y^j}: Y^j \mapsto Y.$$

The proposed LPDh method is now outlined in Algorithm 2. The networks Γ^i and Λ^i have the same architecture but different weights for $i = 1, 2, \dots, M$. However, the same weights are used within the inner loop $j = 1, 2, \dots, N_s$.

Algorithm 2 LPDh

```

1: Choose initial primal and dual variables
    $(f_0, u_0) = \text{init}(g)$ , where  $(f_0, u_0) \in (X^{N_p}, Y^{N_d})$ 
2: For  $i = 1, 2, \dots, M$  do:
3:   For  $j = 1, 2, \dots, N_s$  do:
4:      $k = iN_s + j$ 
5:     Select section:  $\bar{u}_{k-1} = \mathcal{P}_{Y^j}(u_{k-1})$ ,  $\bar{g} = \mathcal{P}_{Y^j}(g)$ .
6:     Select sub-volume:  $\bar{f}_{k-1} = \mathcal{P}_{X^j}(f_{k-1})$ .
7:     Dual:  $u_k = u_{k-1} + \tilde{\mathcal{P}}_{Y^j} \left( \Gamma^i \left( \bar{u}_{k-1}, \mathcal{A}^j \left( \bar{f}_{k-1}^{(2)}, \bar{g} \right) \right) \right)$ 
8:     Primal:  $f_k = f_{k-1} + \tilde{\mathcal{P}}_{X^j} \left( \Lambda^i \left( \bar{f}_{k-1}, (\mathcal{A}^j)^* \left( \bar{u}_{k-1}^{(1)} \right) \right) \right)$ 
9: return  $f_{MN_s}^{(1)}$ 

```

This implies that the method can be applied with different numbers of data sections/line subsets N_s , which means that it can be applied to any length of the helical trajectory.

The difference between LPD and LPDh is that the latter (partially) updates the primal variable after each partial update of the dual variable, while the former fully updates the dual variable and only then updates the primal variable. We empirically compare these two approaches in section 4.3. We chose the section size to be equal to a single half-turn of a helical trajectory, so that back-propagation through one unrolled sub-iteration can be done on a GPU with 24GB of memory. We use slightly smaller CNNs compared to [1]: The number of memory channels for the dual variable are $N_d = 1$ instead of 5 and we use 16 channels instead of 32 in the hidden layers of the dual mapping Γ^i .

3.3 Training and testing schemes

We train the CNNs Γ^i and Λ^i in LPD and LPDh using data corresponding to k consecutive sections. More precisely, the loss for the training pair (f_i, g_i) is computed as

$$\mathcal{L}_X \left(\mathcal{R}_\theta(\mathcal{P}_{Y^{(q;q+k)}}(g_i)), \mathcal{P}_{X^{(q;q+k)}}(f_i) \right). \quad (4)$$

where \mathcal{L}_X is the standard ℓ_2 -norm and q is a random number from 1 till $N_s - k$. The projection operator defined in the data domain selects k subsequent data sections, i.e. $\mathcal{P}_{Y^{(q;q+k)}} : Y \rightarrow Y^{q;q+k}$ where

$$\mathcal{P}_{Y^{(q;q+k)}}(g) = (g^q, \dots, g^{q+k-1})$$

The projection operator defined in the image domain selects the union of k image sub-volumes corresponding to the data, i.e. $\mathcal{P}_{X^{(q;q+k)}} : X \rightarrow X^{q;q+k}$ where

$$\mathcal{P}_{X^j}(\mathcal{P}_{X^{(q;q+k)}}(f)) = f^{q+j-1} \quad \text{for } j = 1, \dots, k.$$

We hypothesise that this limited training is sufficient for the LPDh to generalize to the case with more sections. This assumption is checked empirically in section 4.3.

An alternative strategy is to apply the method in a “sliding window” manner using the same number of sections as it was trained for. To combine the obtained reconstructions, we compute a weighted average, where a weight for each slice in a sub-volume depends on the distance of this slice to the center of the sub-volume. The further the slice is from the center, the smaller its weight is. More precisely, let us denote the center along the rotation axis of the reconstructed sub-volume with index q by z_c^q and its thickness by z_t^q . Then, the reconstruction \hat{f}_z of the 2D slice f_z is obtained from the independently reconstructed sub-volumes $\hat{f}_z^q = \mathcal{R}_\theta(\mathcal{P}_{Y^{(q;q+k)}}(g))$ for $q = 1, \dots, N_s - k$ as follows:

$$\hat{f}_z = \frac{\sum_{q=1}^{N_s} w_{z,q} \hat{f}_z^q}{\sum_{q=1}^{N_s} w_{z,q}}$$

where

$$w_{z,q} = \begin{cases} 1 - \frac{2}{z_t^q} |z - z_c^q|, & \text{if } |z - z_c^q| \leq z_t^q/2 \\ 0 & \text{otherwise.} \end{cases}$$

4 Experiments and results

First, we use simplified training data to select hyper-parameters and to compare the different approaches described in the previous section in a so-called ablation study. Then, we train the LPDh using realistic training data and perform quantitative comparison to a baseline method. Finally, we evaluate the trained network on the (pre-processed) real clinical data.

4.1 Data

We simulate experimental data using LDCCT data set [25] provided by the Cancer Imaging Archive. Furthermore, we evaluate the proposed methods on the *real* projection data from this data set. The data set contains helical CT scans of 299 patients involving head, thorax, and abdomen acquired using scanners from Siemens Healthcare and GE Healthcare. Due to differences in scanning protocols for different vendors and different body parts, we chose to focus only on scans of the abdomen (45 in total) acquired using a Siemens system. Of these, 40 are used for training, one for validation (‘L134’), and four for testing (‘L072’, ‘L019’, ‘L116’, ‘L150’). For each case, one has full dose and reduced dose (25%) projection data along with corresponding reference 3D reconstructions.

Simulated data for training The 3D reconstructions obtained from full dose CT in the above mentioned data set were used as digital phantoms to generate low-dose helical CT data in the following way. First, the input 3D reconstruction f , which is given in the Hounsfield units, is re-scaled as

$$f = \left(\frac{f_{\text{HU}}}{1000} + 1 \right) \mu_0,$$

where $\mu_0 := 0.0192 \text{ mm}^{-1}$ is the X-ray attenuation of water at the mean X-ray energy of 70 keV. Next, noise-free tomographic data $g = \mathcal{A}(f)$ is simulated using the ray transform with the original acquisition geometry provided together with the data. Next, the data is corrupted by Poisson noise

$$H_{\text{noisy}} = \text{Poisson}\left(H_0 e^{-\mathcal{A}(f)}\right),$$

where H_0 is the number of photons per pixel available with the data. Finally, the data is linearized so that $g \approx \mathcal{A}(f)$ where

$$g = -\ln\left(\frac{1}{H_0} H_{\text{noisy}}\right).$$

The full dose reconstructions included in the data set (our ground truth) are slightly truncated from both ends along the rotation axis comparing to the region that was illuminated to generate the projection data. This is done, because reconstruction in those region is only partial, due to the lack of data from all angles. Therefore, when we simulate the data, we discard source positions in the beginning and at the end of a scan, leaving only those source positions, whose rays cross the ground truth volume and do not cross missing regions.

Simplified geometries for the ablation study In order to perform the ablation experiments in a shorter time frame, we simplify the original acquisition geometries included in the data set by using a flat detector and not using Flying Focal Spot (FFS) (we disregard every second angle).

Real data The simulation process described above is not perfect (even with real acquisition geometries and photon statistics). Hence, in order to apply the reconstruction method trained on simulated data, we need to apply corrections to the real data. First of all, the LDCT reference reconstructions, that we use as phantoms to generate the training data, do not cover objects that are outside the scanner’s field of view, such as cables, blankets, and the table. Therefore, our method is not trained to reconstruct those objects. Secondly, visual examination of the real data shows that for some source angles there appears to be an additive error, which is almost constant along the first detector axis (detector width). This likely comes from normalizing data with incorrect gain estimates [38].

To address both of these issues we seek our own reference reconstruction using the full dose data. Since we don’t have access to other methods we construct a new reference reconstruction by solving the optimization problem:

$$\min_{f,c} \mathcal{L}_Y(\mathcal{A}(f), g + c), \quad (5)$$

where $c \in \mathbb{R}^{N_\varphi \times D_h}$ is a gain correction for each source position and detector row and the data discrepancy $\mathcal{L}_Y: Y \times Y \rightarrow \mathbb{R}$ is a weighted l_2 -norm [10]:

$$\mathcal{L}_Y(\mathcal{A}(f), g) = \sum_{i=1}^{|Y|} w_i \|\mathcal{A}(f)_i - g_i\|_2^2 \quad \text{where } w_i := e^{-g_i}. \quad (6)$$

We solve eq. (5) using Nesterov’s accelerated gradient descent [30] for 200 iterations. We use the obtained reconstruction to correct the real data as follows

$$g_{corr} = g_{real} - \mathcal{A}(\mathcal{M}(\hat{f})) + \hat{c} \quad (7)$$

where $\mathcal{M}: X \rightarrow X$ is a an operator that masks the central part of the reconstruction, so that only the truncated regions are projected, and \hat{f}, \hat{c} are obtained by minimizing eq. (5) as described above.

We hypothesize that the corrections eq. (7) could be (as well) performed using a full (not truncated) weighted FBP reconstruction for \hat{f} and $g - \mathcal{A}(\hat{f})$ averaged along the first detector axis for \hat{c} . Alternatively, the training could be done on full (not-truncated) phantoms.

Lastly, the measured data has much higher resolution in the dimension along the rotation axis than the reference reconstructions. Minimizing data discrepancy eq. (5) for image volumes $f \in X$ that are too coarse results in typical “undershooting” artifacts near structures with high attenuation such as bones. To avoid this, we smooth the data along this dimension by applying a convolution with a normalized triangle filter with half width equal twice the size of reconstructed voxels.

4.2 Implementation details

The proposed method is implemented in Python with specific C++/CUDA based libraries for computationally demanding tasks. An example of the latter is CT-related components, which are implemented in the Operator Discretisation Library (ODL) [2] with ASTRA [41] as back-end for computing forward/back-projections. The neural network layers and training are implemented using PyTorch [32].

The neural networks used in LPD and LPDh are almost identical to the original method [1] regarding structure and hyper-parameters. A three-layer CNN is applied in both image and projection domain at each unrolled iteration, i.e., Λ^i and Γ^i have two hidden convolutional layers with 32 and 16 filters, respectively, and one convolutional output layer. ReLUs are used as activation functions after hidden layers. Training is performed with the Adam optimizer [22] using the ℓ_2 -distance to the ground-truth described in eq. (4). The initial learning rate is set to $5 \cdot 10^{-4}$ with cosine annealing. Since the training samples become larger with the increased number of sections, we define the total number of training iterations to be $2 \cdot 10^5 / (10 + 5 \cdot N_s)$, where $10 + 5 \cdot N_s$ is a rough estimate of the number of slices in a target reconstruction for a given number of sections N_s . However, we use 10^4 iterations, when training with the real geometries.

Theoretically, the size of image sub-spaces X^j depends on the pitch. In practice, the pitch can vary across different scans and also within each scan (we observe values within the range 17.18 mm to 34.5 mm in our training and testing set). The method must therefore be robust w.r.t. these variations, assuming they are not too big. For simplicity, we set $N_t = 16$, which is a suitable value for most of the scans.

Quantitative performance of all methods is measured by calculating the peak signal to noise ratio (PSNR) and the structural similarity index (SSIM) between the ground truth image and its corresponding reconstruction. However, since the data is truncated at the beginning and the end of acquisition geometry, we discard first 8 and last 8 reconstructed 2D slices, since reconstruction in those regions is only partial.

Baseline method We compare our approach to a variational model with Huber regularizer, i.e., reconstruction obtained from $\mathcal{R}_\theta: Y \rightarrow X$ that is defined as

$$\mathcal{R}_\theta(g) \in \arg \min_f \left\{ \mathcal{L}_Y(\mathcal{A}(f), g) + \lambda \mathcal{S}_\theta(f) \right\}. \quad (8)$$

Here, the data discrepancy is given as in eq. (6) and the regularizer $\mathcal{S}_\theta: X \rightarrow \mathbb{R}$ is smooth relaxation of the non-smooth ℓ_1 -norm that makes up the total variation (TV) regularizer [16]:

$$\mathcal{S}_\theta(f) := \sum_{i=1}^{2|X|} h_\theta(|\nabla f_i|) \quad \text{where } h_\theta(t) := \begin{cases} t^2/(2\theta), & t \leq \theta \\ t - \theta/2, & t > \theta. \end{cases}$$

In our experiments, we set the regularization parameter and the Huber parameter to $\lambda = 0.15$ and $\theta = 0.0012$, respectively. The optimization in eq. (8) is solved using Nesterov’s accelerated gradient descent [30] that is stopped (early) after 200 iterations. We initialize the optimization with an approximate FBP algorithm implemented in ODL, which does not account for FFS. We chose the hyper-parameters and the number of iterations that lead to optimal performance on the validation data. In particular, early stopping does not only improve upon computational feasibility, it has also been shown to provide an additional regularising effect as outlined in [9].

4.3 Ablation study

In this section we empirically compare the methods described in section 3. Since training of the neural networks on a single high-end consumer GPU takes weeks, we use data simulated using simplified geometries (as described in section 4.1). In section 4.3 we evaluate the performance of LPD and LPDh trained with different number of sections.

First of all, we can see that LPDh unambiguously outperforms LPD without increase in total computational time for inference. Secondly, both LPD and LPDh perform poorly, if trained only using 2 subsequent sections. In this cases, it is much more beneficial to apply the method in a sliding window manner. However, as the number of sections during the training increases, the generalization to an unlimited number of sections (25–72 in our test cases) improves greatly. If 6 sections are used, there is almost no difference in performance between the sliding window testing strategy and the regular forward pass, suggesting that almost perfect generalization is achieved in this case. Ultimately,

we can see that LPDh with 6 sections provides very good performance without a relevant increase in estimation time. Still, the best performing approach is LPDh trained with 4 sections and tested in sliding window manner. We evaluate the latter in the next sections using realistic simulated data and real data.

	PSNR	SSIM	time, min
LPD, 2 sections	28.74	0.524	9.9
LPD, 2 sections, sliding window	39.61	0.964	23.5
LPDh, 2 sections	24.94	0.477	9.9
LPDh, 2 sections, sliding window	40.88	0.972	19.1
LPD, 4 sections	38.83	0.957	9.9
LPD, 4 sections, sliding window	39.56	0.964	44.1
LPDh, 4 sections	40.59	0.970	9.7
LPDh, 4 sections, sliding window	41.37	0.975	35.9
LPD, 6 sections	39.52	0.962	9.7
LPD, 6 sections, sliding window	39.86	0.966	64.2
LPDh, 6 sections	40.95	0.972	10.2
LPDh, 6 sections, sliding window	41.02	0.974	52.4

Tab. 1: Performance metrics for LPD and LPDh using different number of sections during training. Averages over four test patients are reported.

4.4 Results

We here evaluate LPDh with 4 sections, since it showed the best performance in section 4.3. It is trained against simulated data with geometries and noise levels that correspond to those in the LDCT data set. Table 2 lists quantitative performance results in terms of PSNR and SSIM as well as average execution time. LPDh clearly outperforms the baseline Huber regularization, while being an order of magnitude faster.

	PSNR	SSIM	time, min
Huber reg.	44.65	0.981	720
LPDh	45.80	0.986	40
LPDh, sliding window	46.19	0.987	127

Tab. 2: Performance metrics for different reconstruction methods on realistic data. Averages over four test patients are reported.

Next, we perform visual comparison of the proposed methods applied to the real data (corrected as described in section 4.1) in fig. 3. We present two baseline reconstructions: the low dose reference included in the data set and the iterative reconstruction with Huber regularization. We also show two full dose reconstructions: one that is included in the data set and our own reference obtained from the full dose data by addressing problem eq. (5).

5 Limitations

We do not present a quantitative comparison of reconstructions obtained from the real data. The reason is that the LDCT full dose reference does not represent the actual “ground truth” with sufficient accuracy. Figure 3 shows that the iterative reconstruction computed in a time-unconstrained setting seems to provide a superior recovery of small details. However, it does not mean that the quality of our reference reconstruction cannot be challenged. It is, e.g., likely to contain more noise than the LDCT full dose reference. We are therefore hesitant to use it as the ground truth.

Yet another issue that undermines quantitative comparison is that full dose and low dose reconstructions obtained with the same method will have additional similarities that result from implicit/explicit prior information imposed by the method, let’s call it method’s bias. Thus, the low dose FBP reconstruction is closer in PSNR to the full dose FBP reconstruction, while iterative reconstructions, Huber regularization and LPDh, are closer to the iterative full dose reconstruction (our full dose reference).

Furthermore, the issues described above should be accounted for when training the method in a supervised manner with the real data. We tried to train LPDh using the LDCT full dose reference, but the performance was similar (slightly worse) to U-Net post-processing of the low dose reference. Nevertheless, we have seen in figure fig. 3 that the full dose reference does not contain all the details that LPDh is able to reconstruct after being trained on *simulated* data. Moreover, quantitative comparison confirms that LPDh reconstructions are closer to our own reference than both LDCT reference reconstructions. One option would be to train LPDh using full dose iterative reconstructions as proxies for ground truth. However, obtaining such reconstructions for the whole data set requires a lot of computational resources and the quality of reconstruction would still be questioned.

To summarize, it is clear that there are differences between full dose reconstructions obtained with different methods. Furthermore, none of the methods can perfectly recover the actual “ground truth”. Obtaining a good proxy for the ground truth using full dose data in a time-unconstrained setting requires a separate investigation, which should be ideally performed by the maintainers of LDCT data set. An alternative approach is to avoid defining a ground truth and consider quality metrics based on the data discrepancy in the projection domain. This was done in [23] where some randomly selected projections are left out during the reconstruction process, so that they can be used to compute the unsupervised data discrepancy loss.

The final limitation is the lack of freely available software suitable for reconstructing the clinical CT data, in particular the ones from the LDCT challenge. For instance, the open source software library *FreeCT* [14] that implements the weighted Filtered Back Projection (wFBP) algorithm from [36] currently does not support FFS. As a consequence, we used iterative reconstruction with Huber regularizer as the baseline method, even though the method is not practical due to its execution time. Like all iterative reconstruction algorithms, LPDh

is computationally much more demanding than analytic methods and thus inherently slower. However, keeping in mind that iterative methods are clinically available and that the learned components account only for 12% of our total execution time, this aspect should not prevent the method from clinical use. Finally, it is possible that with a good initialization of LPDh method (instead of zero-initialization) the number of unrolled iterations could be reduced. Such initialization could be applied if high quality analytic methods, such as the ones used by vendors, were available.

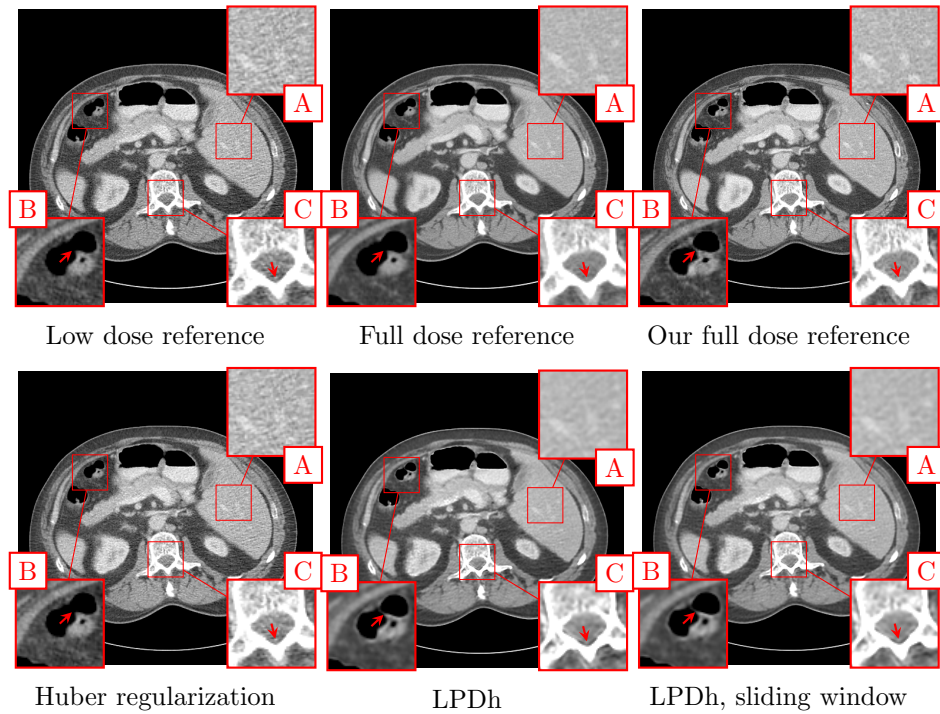


Fig. 3: Transverse cross section of 3D reconstructions obtained from different methods (level 0 HU, window 400 HU). Full dose reference and our reference are obtained from full dose data and serve as proxies for “ground truth”. Region (A) shows improved denoising with LPDh methods. Region (B) shows reconstruction of small high contrast structures. We can see that LPDh shows the connective tissue in contrast to the full dose reference included in the data set. Examination of our own full dose reference (obtained through iterative reconstruction) reveals that this is not a mistake. Region (C) shows that LPDh methods still suffer from undershooting artifacts, which were almost (but not fully) removed by smoothing the data as described in section 4.1.

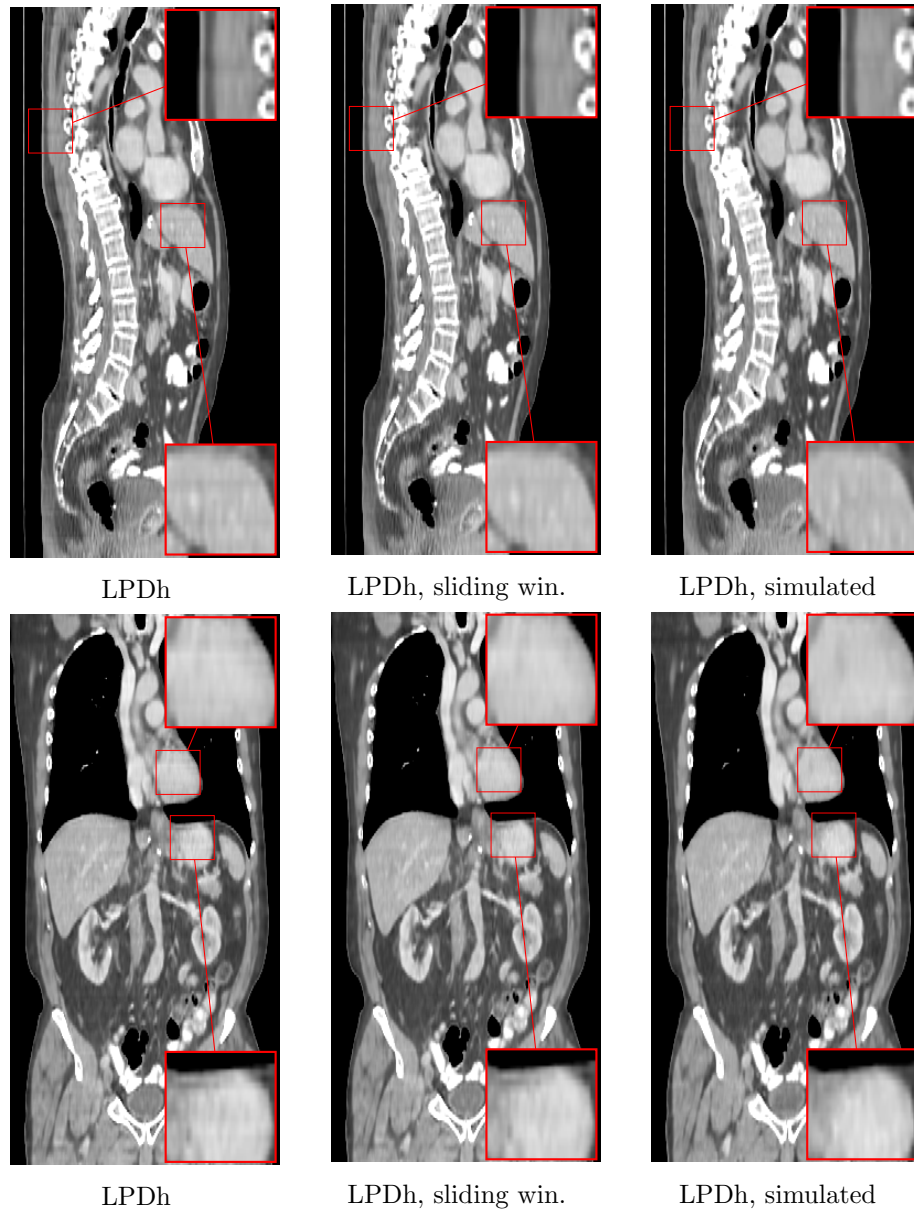


Fig. 4: Sagittal and coronal cross sections of 3D reconstructions obtained with LPDh (level 0 HU, window 400 HU) from the real and simulated data. Splitting of the image volume during the reconstruction leads to subtle horizontal streak artifacts, which are less noticeable in the reconstruction obtained in a sliding window manner. The remaining small differences between simulated and the real data seems to be partially responsible for the appearance of the artifacts, since the artifacts are almost invisible in the reconstructions from the simulated data.

6 Conclusions

We have proposed LPDh – a new algorithm in the family of Learned Primal-Dual methods that is suited for the reconstruction of helical CT data. We overcome the main challenge – large GPU memory requirements of the original LPD method, and train LPDh on a *single consumer GPU*.

To achieve this, we address the problem on several levels. First is to apply gradient check-pointing to unrolled iterations. Second is to split geometry and data into sections, so that an unrolled iteration w.r.t. one section fits the GPU memory. Finally, we train the method on smaller samples of the data that correspond to a few helical turns. Although our method generalizes very well to the data that is an order of magnitude larger than the training samples, we find that applying the method in a sliding window manner can additionally boost the performance at the cost of computational time.

Training and quantitative performance evaluation has been done on data from realistic simulations. Qualitative performance has been assessed on clinical data from the LDCT data set.

7 Acknowledgements

The computations were partially enabled by resources provided by the National Academic Infrastructure for Supercomputing in Sweden (NAISS) at Chalmers partially funded by the Swedish Research Council through grant agreement no. 2022-06725.

References

- [1] J. Adler and O. Öktem. Learned primal-dual reconstruction. *IEEE Transactions on Medical Imaging*, 37(6):1322–1332, 2018.
- [2] Jonas Adler, Holger Kohr, and Ozan Öktem. Operator discretization library (ODL), 2017.
- [3] Sangtae Ahn, Jeffrey A Fessler, Doron Blatt, and Alfred O Hero. Convergent incremental optimization transfer algorithms: Application to tomography. *IEEE Transactions on Medical Imaging*, 25(3):283–296, 2006.
- [4] S. Arridge, P. Maass, O. Öktem, and C.-B. Schönlieb. Solving inverse problems using data-driven models. *Acta Numerica*, 28:1–174, 2019.
- [5] C. Bontus and T. Köhler. Reconstruction algorithms for computed tomography. *Advances in Imaging and Electron Physics*, 151:1–63, 2009.
- [6] Antonin Chambolle and Thomas Pock. A First-Order Primal-Dual Algorithm for Convex Problems with Applications to Imaging. *Journal of mathematical imaging and vision*, 40(1):120–145, 2011.

-
- [7] Ricky TQ Chen, Yulia Rubanova, Jesse Bettencourt, and David K Duvenaud. Neural ordinary differential equations. *Advances in neural information processing systems*, 31, 2018.
 - [8] Tianqi Chen, Bing Xu, Chiyuan Zhang, and Carlos Guestrin. Training deep nets with sublinear memory cost. *arXiv*, 1604.06174, 2016.
 - [9] Alexander Effland, Erich Kobler, Karl Kunisch, and Thomas Pock. Variational networks: An optimal control approach to early stopping variational methods for image restoration. *Journal of mathematical imaging and vision*, 62(3):396–416, 2020.
 - [10] Idris A Elbakri and Jeffrey A Fessler. Statistical image reconstruction for polyenergetic X-ray computed tomography. *IEEE Transactions on Medical Imaging*, 21(2):89–99, 2002.
 - [11] Hakan Erdogan and Jeffrey A Fessler. Ordered subsets algorithms for transmission tomography. *Physics in Medicine & Biology*, 44(11):2835, 1999.
 - [12] Aidan N Gomez, Mengye Ren, Raquel Urtasun, and Roger B Grosse. The reversible residual network: Backpropagation without storing activations. *Advances in neural information processing systems*, 30, 2017.
 - [13] Andreas Hauptmann, Jonas Adler, Simon R Arridge, and Ozan Öktem. Multi-scale learned iterative reconstruction. *IEEE Transactions on Computational Imaging*, 2020.
 - [14] John Hoffman, Stefano Young, Frédéric Noo, and Michael McNitt-Gray. FreeCT_wFBP: a robust, efficient, open-source implementation of weighted filtered backprojection for helical, fan-beam CT. *Medical Physics*, 43(3):1411–1420, 2016.
 - [15] J. Hsieh, B. Nett, Z. Yu, K. Sauer, J.-B. Thibault, and C. A. Bouman. Recent advances in CT image reconstruction. *Current Radiology Reports*, 1:39–51, 2013.
 - [16] Peter J Huber. *Robust statistics*, volume 523. John Wiley & Sons, 2004.
 - [17] H. M. Hudson and R. S. Larkin. Accelerated image reconstruction using ordered subsets of projection data. *IEEE Transactions on Medical Imaging*, 13(4):601–609, 1994.
 - [18] Kyong Hwan Jin, Michael T McCann, Emmanuel Froustey, and Michael Unser. Deep convolutional neural network for inverse problems in imaging. *IEEE Transactions on Image Processing*, 26(9):4509–4522, 2017.
 - [19] A. Katsevich. A general scheme for constructing inversion algorithms for cone beam CT. *International Journal of Mathematics and Mathematical Sciences*, 2003(21):1305–1321, 2003.

-
- [20] A. Katsevich. 3PI algorithms for helical computer tomography. *Advances in Applied Mathematics*, 36(3):213–250, 2006.
- [21] Donghwan Kim, Sathish Ramani, and Jeffrey A Fessler. Combining ordered subsets and momentum for accelerated X-ray CT image reconstruction. *IEEE Transactions on Medical Imaging*, 34(1):167–178, 2014.
- [22] D. P. Kingma and J. Ba. Adam: A method for stochastic optimization. *arXiv preprint*, 1412.6980, 2014.
- [23] Onni Kosomaa, Samuli Laine, Tero Karras, Miika Aittala, and Jaakko Lehtinen. Simulator-based self-supervision for learned 3d tomography reconstruction. *arXiv*, 2212.07431, 2022.
- [24] Marinus J Lagerwerf, Daniël M Pelt, Willem Jan Palenstijn, and Kees Joost Batenburg. A computationally efficient reconstruction algorithm for circular cone-beam computed tomography using shallow neural networks. *Journal of Imaging*, 6(12):135, 2020.
- [25] C. McCollough, B. Chen, D. R. Holmes III, X. Duan, Z. Yu, L. Yu, S. Leng, and J. Fletcher. Low dose CT image and projection data (LDCT-and-Projection-data) (version 5) [data set]. The Cancer Imaging Archive, 2020.
- [26] A. Mileto, L. S. Guimaraes, C. H. McCollough, J. G. Fletcher, and L. Yu. State of the art in abdominal CT: The limits of iterative reconstruction algorithms. *Radiology*, 293(3):491–503, 2019.
- [27] Vishal Monga, Yuelong Li, and Yonina C Eldar. Algorithm unrolling: Interpretable, efficient deep learning for signal and image processing. *IEEE Signal Processing Magazine*, 38(2):18–44, 2021.
- [28] N Moriakov, JJ Sonke, and J Teuwen. End-to-end memory-efficient reconstruction for cone beam ct. *Medical Physics*, 2023.
- [29] Naveen Murthy and Jeffrey A Fessler. Block axial checkerboarding: A distributed algorithm for helical X-ray CT reconstruction. In *2020 IEEE 17th International Symposium on Biomedical Imaging (ISBI)*, pages 191–194. IEEE, 2020.
- [30] Yurii E Nesterov. A method for solving the convex programming problem with convergence rate $o(1/k^2)$. In *Proceedings of the USSR Academy of Sciences (Doklady Akademii Nauk SSSR)*, volume 269, pages 543–547, 1983.
- [31] Frédéric Noo, Michel Defrise, and Rolf Clackdoyle. Single-slice rebinning method for helical cone-beam CT. *Physics in Medicine & Biology*, 44(2):561, 1999.

-
- [32] Adam Paszke, Sam Gross, Soumith Chintala, Gregory Chanan, Edward Yang, Zachary DeVito, Zeming Lin, Alban Desmaison, Luca Antiga, and Adam Lerer. Automatic differentiation in PyTorch. In *31st Conference on Neural Information Processing Systems (NIPS 2017), Long Beach, CA, USA*, 2017.
- [33] Patrick J. La Riviere and Carl R. Crawford. From EMI to AI: a brief history of commercial CT reconstruction algorithms. *Journal of Medical Imaging*, 8(5):39–51, 2021.
- [34] Jevgenija Rudzusika, Buda Bajić, Ozan Öktem, Carola-Bibiane Schönlieb, and Christian Etmann. Invertible learned primal-dual. In *NeurIPS 2021 Workshop on Deep Learning and Inverse Problems*, 2021.
- [35] O. Scherzer, M. Grasmair, H. Grossauer, M. Haltmeier, and F. Lenzen. *Variational methods in imaging*, volume 167 of *Applied Mathematical Sciences*. Springer, 2009.
- [36] Karl Stierstorfer, Annabella Rauscher, Jan Boese, Herbert Bruder, Stefan Schaller, and Thomas Flohr. Weighted FBP—a simple approximate 3D FBP algorithm for multislice spiral CT with good dose usage for arbitrary pitch. *Physics in Medicine & Biology*, 49(11):2209, 2004.
- [37] Junqi Tang. Stochastic primal-dual deep unrolling networks for imaging inverse problems. *arXiv*, 2110.10093, 2021.
- [38] Jean Baptiste Thibault, Zhou Yu, Ken Sauer, Charles Bouman, and Jiang Hsieh. Correction of gain fluctuations in iterative tomographic image reconstruction. In *Proc. Intl. Mtg. on Fully 3D Image Recon. in Rad. and Nuc. Med.*, pages 112–5, 2007.
- [39] Mareike Thies, Fabian Wagner, Mingxuan Gu, Lukas Folle, Lina Felsner, and Andreas Maier. Learned cone-beam CT reconstruction using neural ordinary differential equations. In *7th International Conference on Image Formation in X-Ray Computed Tomography*, volume 12304, pages 48–54. SPIE, 2022.
- [40] H. Turbell. *Cone-Beam Reconstruction Using Filtered Backprojection*. Phd thesis, Department of Electrical Engineering, Linköpings universitet, Linköpings, Sweden, 2001.
- [41] Wim Van Aarle, Willem Jan Palenstijn, Jeroen Cant, Eline Janssens, Folkert Bleichrodt, Andrei Dabrovolski, Jan De Beenhouwer, K Joost Batenburg, and Jan Sijbers. Fast and flexible X-ray tomography using the AS-TRA toolbox. *Optics Express*, 24(22):25129–25147, 2016.
- [42] Fabian Wagner, Mareike Thies, Laura Pfaff, Oliver Aust, Sabrina Pechmann, Daniela Weidner, Noah Maul, Maximilian Rohleder, Mingxuan Gu, Jonas Utz, et al. On the benefit of dual-domain denoising in a self-supervised low-dose CT setting. *arXiv*, 2211.01111, 2022.

-
- [43] M. J. Willeminck and P. B. Noël. The evolution of image reconstruction for CT — from filtered back projection to artificial intelligence. *European Radiology*, 29:2185—2195, 2019.
- [44] Dufan Wu, Kyungsang Kim, and Quanzheng Li. Computationally efficient deep neural network for computed tomography image reconstruction. *Medical Physics*, 46(11):4763–4776, 2019.